The British Journal of Radiology, 84 (2011), 526–533

Micro-CT enables microlocalisation and quantification of Her2-targeted gold nanoparticles within tumour regions

[1]J F HAINFELD, PhD, [1]M J O'CONNOR, [2]F A DILMANIAN, PhD, [1]D N SLATKIN, MD, [3]D J ADAMS, PhD and [4]H M SMILOWITZ, PhD

[1]*Nanoprobes, Inc., 95 Horseblock Rd, Yaphank, NY 11980, USA,* [2]*Department of Radiation Oncology, State University of New York at Stony Brook, Health Sciences Center, Stony Brook, NY 11794-7028, and Brookhaven National Laboratory, Medical Department, Bldg. 490, 30 Bell Ave., Upton, NY 11973-5000, USA,* [3]*Department of Orthopaedic Surgery, and* [4]*Department of Cell Biology, University of Connecticut Health Center, 263 Farmington, CT 06030, USA*

Objectives: Gold nanoparticles are of interest as potential *in vivo* diagnostic and therapeutic agents, as X-ray contrast agents, drug delivery vehicles and radiation enhancers. The aim of this study was to quantitatively determine their targeting and microlocalisation in mouse tumour models after intravenous injection by using micro-CT.
Methods: Gold nanoparticles (15 nm) were coated with polyethylene glycol and covalently coupled to anti-Her2 antibodies (Herceptin). *In vitro*, conjugates incubated with Her2+ (BT-474) and Her2– (MCF7) human breast cancer cells showed specific targeted binding with a Her2+ to Her2– gold ratio of 39.4 ± 2.7:1. Nude mice, simultaneously bearing subcutaneous Her2+ and Her2– human breast tumours in opposite thighs were prepared. Gold nanoparticles alone, conjugated to Herceptin or to a non-specific antibody were compared. After intravenous injection of the gold nanoparticles, gold concentrations were determined by atomic absorption spectroscopy. Microlocalisation of gold was carried out by calibrated micro-CT, giving both the radiodensities and gold concentrations in tumour and non-tumour tissue.
Results: All gold nanoparticle constructs showed accumulation, predominantly at tumour peripheries. However, the Herceptin–gold nanoparticles showed the best specific uptake in their periphery (15.8 ± 1.7% injected dose per gram), 1.6-fold higher than Her2– tumours and 22-fold higher than surrounding muscle. Imaging readily enabled detection of small, 1.5 mm-thick tumours.
Conclusion: In this pre-clinical study, antibody-targeted 15 nm gold nanoparticles showed preferential uptake in cognate tumours, but even untargeted gold nanoparticles enhanced the visibility of tumour peripheries and enabled detection of millimetre-sized tumours. Micro-CT enabled quantification within various regions of a tumour.

Received 27 August 2009
Revised 22 October 2009
Accepted 14 December 2009

DOI: 10.1259/bjr/42612922

Antibodies bound to conventional iodine CT contrast agents have not provided sufficient targeted CT contrast since they only load around three iodine atoms per antibody. However, gold nanoparticles (AuNPs) can load antibodies with a greater number of heavier atoms. A 15 nm AuNP contains approximately 100 000 gold atoms, thus promising to provide useful X-ray contrast for targeted tumours [1, 2]. AuNPs have been shown to confer designable blood half-lives from several minutes [3] to 15 h [2], making them interesting X-ray vascular imaging agents. Their blood half-lives are longer than iodine agents and promote better tumour uptake. Optical *in vivo* imaging has been achieved using near-infrared optical coherence tomography [4] or surface-enhanced Raman spectroscopy [5]. If tumours are targeted with AuNPs, they can be used for drug delivery [6], near-infrared hyperthermia ablation [4, 7] or enhancement of radiotherapy [8–11]. However, the microlocalisation of AuNPs in tumours after intravenous (iv) injection has not been extensively studied. In this report, we quantify tumour loading by Herceptin-targeted and untargeted AuNPs in mice using micro-CT and atomic absorption spectroscopy. Trastuzumab (Herceptin) is a humanised monoclonal antibody currently used to treat human breast cancers with upregulated Her2 (human epidermal growth factor receptor 2) expression, which occurs in approximately 30% of breast cancer patients [12]. Tumour contrasting could be useful for early detection and visualising a tumour's true extent to assist in image-guided surgeries, radiotherapy planning, non-invasive tumour typing, detection of lymph node involvement, drug, infrared and X-ray therapies, and monitoring.

Address correspondence to: Dr James F. Hainfeld, Nanoprobes, Inc., 95 Horseblock Rd, Yaphank, NY 11980, USA, E-mail: hainfeld@nanoprobes.com

Methods and materials

Gold nanoparticles

15 nm AuNPs were synthesised by sodium citrate reduction in boiling water [13]. AuNPs were coated with thio-polyethylene glycol-COOH (thio-PEG-COOH)

(3000 MW, Rapp Polymere, Tübingen, Germany) [14]. These were linked to Herceptin (Genentech, South San Francisco, CA) or mouse immunoglobulin G (IgG, Sigma, St Louis, MO) using 1-ethyl-3-(3′-(dimethylamino)propyl)-carbodiimide (EDC) and *N*-hydroxysuccinimide (Sigma) [15]. Purification and concentration proceeded by centrifugation (16 kg, 11 min) and ultrafiltration (Amicon Ultra 100 kD, Millipore, Billerica, MA). AuNPs were suspended in phosphate-buffered saline, pH 7.4.

Gold concentrations were quantified by graphite furnace atomic absorption spectroscopy [3] using a Perkin Elmer 4100Z (Waltham, MA).

In vitro *studies*

Human breast cancer cell lines BT474 and MCF-7 (ATCC, Manassas, VA) were grown to 50–70% confluence in T75 flasks (Sarstedt, Newton, NC) in complete Dulbecco's modified Eagle medium (DMEM, GIBCO 11995, North Andover, MA)-based culture medium consisting of DMEM supplemented with 10% fetal bovine serum (Atlanta Biologicals Cat. #S11550, Lawrenceville, GA), glutamine (2 mM), Penn/Strep (100 U ml^{-1}/100 μg ml^{-1}), Fungizone (0.25 μg ml^{-1}), amphotericin B (0.205 μg ml^{-1}) and sodium deoxycholate (all from Invitrogen, Grand Island, NY).

For binding studies, cells were removed from tissue culture flasks with a 0.05% trypsin solution (Invitrogen) and resuspended in L15-based medium containing 10% fetal bovine serum, glutamine and Penn/Strep, then incubated at 37°C with shaking (150 rpm) for 4–5 h. 10^5 to 2×10^6 cells were suspended in 0.5 ml. Either AuNPs or AuNP–Herceptin (1, 10 and 20 optical density $(OD)_{525}$) was added to a final volume of 1 ml. Each concentration was run in duplicate. To competitively assess non-specific binding of AuNP–Herceptin, unlabelled Herceptin (0–12.5 μg) was incubated with cells for 1 h prior to the addition of 1.0 OD_{525} AuNP–Herceptin. Cells were incubated with AuNP–Herceptin for 17 h at 37°C with constant shaking (150 rpm). Cells were washed 5 times at 1500 rpm; each wash was for 5 min in 1 ml of phosphate-buffered saline (GIBCO, 10010). A control of AuNPs only was included to validate that they were not pelleted during the washing centrifugation step.

Animals

Animal experiments were conducted according to National Institutes of Health guidelines and approved by the institutional animal care and use committee before the start of the study.

Slow-release oestrogen pellets made in house [16, 17] were implanted subcutaneously in the scruff of the back in order to stimulate growth of these oestrogen-dependent breast tumours [18]. 1 day after pellet implantation, 10^7 BT474 or MCF-7 tumour cells in 100 μl were mixed with 50 μl of Matrigel (BD Biosciences #354234, San Diego, CA) and injected subcutaneously in opposite thighs in 10-week-old female 01B74-Athymic NCr-nu/nu mice (Charles River, Kingston, NY). 5 days after cell injections, when tumours were approximately 60 mm^3, the mice were injected intravenously via the tail vein (0.2 ml) with AuNPs, AuNP–mouse IgG or AuNP–Herceptin.

Micro-CT

20 h after iv injection, mice were killed and immediately imaged by micro-CT (Scanco Medical AG μCT40 or Scanco VivaCT40, Bruttisellen, Switzerland). The source spot size was 5 μm at 45 kVp (with 0.5 mm Al filtering), sampling with 15 × 15 × 15 μm voxels in a 30 mm-diameter field. 3 mm stacks of 200 sections at 2000 projections per revolution and an integration time of 300 ms per projection were collected, each stack requiring 20 min. After imaging, animals were dissected and tissues were measured for gold content by atomic absorption spectroscopy.

Radiodensity measurements

Radiodensity calibration (Hounsfield units, HU) was carried out by imaging water, normal mice (without gold), various aqueous concentrations of sodium iodide, Omnipaque, $HAuCl_4$ and 15 nm AuNPs. HU values were calculated from images by the formula HU = 1000 × (image intensity – image intensity of water)/(image intensity of water). Gold concentration in tissues was calculated by first subtracting the HU of muscle without gold (measured to be 72) from the HU of the tissue to be measured, then looking up the gold concentration from a plot of the HU of various known concentrations of gold solutions (Figure 1) using the fitted equation (Equation 1).

Image analysis and presentation was done using Amira (Mercury Computer Systems, Chelmsford, MA). At least five measurements were used to determine averages and data spread reported as ± standard deviation (SD) or ± standard error of the mean (SEM) as noted.

Results

In vitro cell binding

Two human breast cancer lines were studied: BT474, which highly expresses the Her2 receptor, and MCF7, which does not; the latter was used as a negative control. After incubation with the Herceptin–AuNPs and washing, the specific uptake of gold (red in colour) was evident from the cell pellets (Figure 2a). Atomic absorption spectroscopy quantitatively revealed that after incubation with 20 OD_{525} AuNP–Herceptin, the Her2+ cells took up 6.9 ± 0.3 μg (mean ± SD) of gold per 5×10^5 cells, equating to 430 000 AuNPs per cell. The Her2– cell line had taken up 0.17 ± 0.01 μg of gold per 5×10^5 cells, yielding a Her2+ to Her2– gold content ratio of 40.1:1. Incubation with lower amounts of gold, 1 and 10 OD_{525} AuNP–Herceptin, led to a similar Her2+ to Her2– gold ratio of 39.4 ± 2.7 (SD, n=4). Competition with unlabelled Herceptin (18 nM) abolished gold uptake (Figure 2b).

In vivo studies

After iv injection of 15 nm AuNPs coupled with Herceptin into nude mice simultaneously bearing both Her2+ and Her2– subcutaneous tumours in opposite

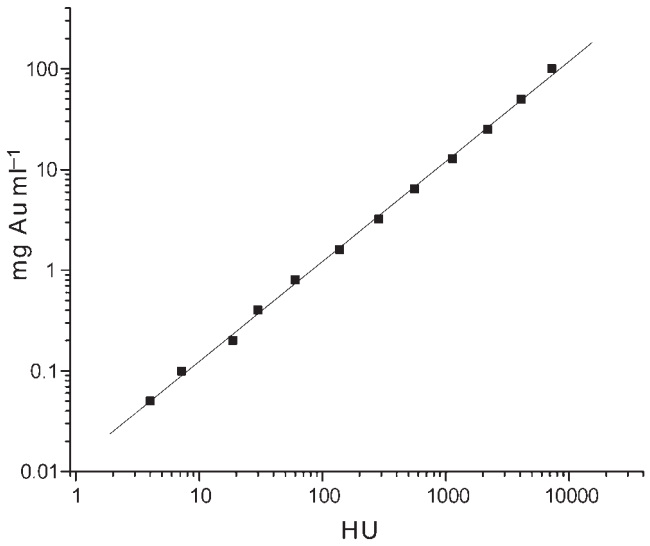

Figure 1. Plot of gold concentration *vs* radiodensity (HU) for the micro-CT used (45 kVp, 0.5 mm Al).

thighs (Figure 3a), specific AuNP accumulation could be detected visually (Figure 3b,c) in the tumours.

Micro-CT was used to find the microlocalisation of the injected gold. The micro-CT was first calibrated with known concentrations of gold solutions. A plot of the radiodensity (HU) *vs* gold concentration is shown in Figure 1.

The data were fit to the line:

$$\log\left(\text{gold concentration}\left(\text{mg Au ml}^{-1}\right)\right) = -1.899\,93 + 0.993\,51 \times \log\left(\text{HU}\right) \quad (1)$$

giving a least squares correlation of 0.999 36. For example, 100 HU corresponds to a gold concentration of 1.22 mg Au ml^{-1}. This is also reasonable since for 45 kVp, the median energy is approximately 20 keV. Using the known X-ray absorption coefficients of gold and water at that energy (μ/ρ) [19], the radiodensity is calculated to be:

$$\begin{aligned}\text{HU} &= 1000 \times (\mu/\rho_{\text{Au}} - \mu/\rho_{\text{water}})/(\mu/\rho_{\text{water}}) \\ &= 1000 \times \left(78.83 \times 0.0012\,2\,\text{g ml}^{-1}/0.8096\right) \\ &= 119\end{aligned} \quad (2)$$

which is close to the measured value of 100 HU.

Mice were then imaged by micro-CT (20 h after iv injection), and results from five different animals are shown in Figure 4. All tumours exhibited radiodense peripheries with a high concentration of gold forming a shell around the tumours. Penetration into the central part of the tumour was poor, giving little contrast. The Her2+ tumour appeared to accumulate somewhat more gold than the Her2– tumour. However, the tumour to surrounding non-tumour ratio was visibly high. Quantification of the gold amounts was also done by atomic absorption spectroscopy. However, atomic absorption spectroscopy is limited to dissected bulk tissues, whereas an advantage of the micro-CT is that measurements can be made on a much finer scale and the microdistribution of the gold can be precisely quantified. Tumours were segmented into the bright gold-laden radiodense periphery, the tumour centre and the whole tumour. Results are shown in Table 1. Data for each tumour were integrated over the whole tumour (not just measured from one section).

Measurements from the subsequently dissected tissues analysed by atomic absorption spectroscopy agreed to within 20% of the values obtained by micro-CT. However, at low gold levels, the atomic absorption spectroscopy measurement was more accurate, since the spectrometer has ppb (parts per billion) sensitivity, whereas for micro-CT the no-gold tissue image intensity (from an uninjected mouse) is subtracted from the low-gold tissue image intensity (both being large numbers compared with their difference), leading to more uncertainty and error. The muscle values from atomic absorption spectroscopy were therefore used in Table 1.

These results show that the whole tumours concentrate the AuNPs, with a Her2+ tumour uptake of $8.3 \pm 1.3\%$ injected dose (id) g^{-1} and Her2– tumour uptake of $6.2 \pm 1.6\%$ id g^{-1}. However, the radiodense tumour peripheries show almost double this localisation, yielding $15.8 \pm 1.7\%$ id g^{-1} for the Her2+ tumour and $10.1 \pm 1.6\%$ id g^{-1} for the Her2– tumour. With either tumour, the tumour to non-tumour (muscle) ratio is quite high, reaching 21.8:1 for the Her2+ periphery: muscle. The centres of the tumours had low gold concentrations, confirming the poor penetration into tumour centres. The actual concentration of gold in the tumour of course depends on the amount injected. For example, a 20 g mouse injected with 1.1 g Au kg^{-1} had the following Her2+ gold concentrations: whole tumour: 1.82 mg Au ml^{-1} (1000×1.1 g Au $kg^{-1} \times 0.02$ kg $\times 8.27\%$ id g^{-1}, 0.182% Au by weight, 159 HU); tumour periphery, 3.48 mg Au ml^{-1} (0.348% Au, 310 HU); muscle, 0.16 mg Au ml^{-1} (0.016% Au, 15 HU). Using the periphery values and Wilcoxon non-parametric analysis, the Her2+ tumour could be distinguished from the Her2– tumour with a p value <0.05.

Several additional controls were performed: (a) mice with an injection of AuNPs only (no antibody), (b) mice with an injection of AuNPs conjugated to a non-specific

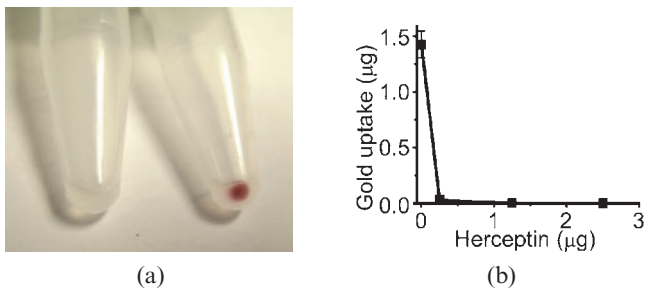

Figure 2. (a) 10^7 human breast cancer cells from a non-Her-2 expressing cell line (MCF7, left) or highly expressing cell line (BT474, right). 15 nm Herceptin conjugate was incubated with each cell line for 17 h, then washed several times. The gold is red and showed obvious specific cell uptake. (b) Competition experiment: cell binding of 15 nm gold Herceptin to BT474 cells with increasing amounts of unlabelled Herceptin. Even at low levels of Herceptin, uptake was virtually eliminated. Error bars for low values are too small to be seen on this graph.

(a) (b) (c)

Figure 3. (a) Mouse model with two implanted tumours: Her2+ in one thigh and Her2– in the contralateral thigh. (b,c) The same mouse with a Her2– tumour (b) and Her2+ tumour (c) 20 h after 0.45 g Au kg^{-1} body weight of 15 nm AuNP–Herceptin intravenous injection. Tumour volumes (by caliper measurements) were nearly identical, but a distinction can be seen owing to the targeted gold localisation. Bar=5 mm.

antibody (mouse IgG) and (c) no AuNPs injected. Typical results are shown in Figure 5 and summarised in Table 2. From these controls, it appears there is no specific preference for either tumour, for either AuNPs only or non-specific IgG-AuNPs, since the Her2+ to Her2– ratios are approximately 1. However, the reasonably high uptake into the tumour peripheries of the AuNPs only (without antibody) suggests that these alone give good tumour distinction for both tumours. The AuNPs showed a tumour periphery to muscle ratio of 22.2 $\pm$ 0.8:1. However, without any AuNPs, the tumours could not be clearly identified by micro-CT (Figure 5c).

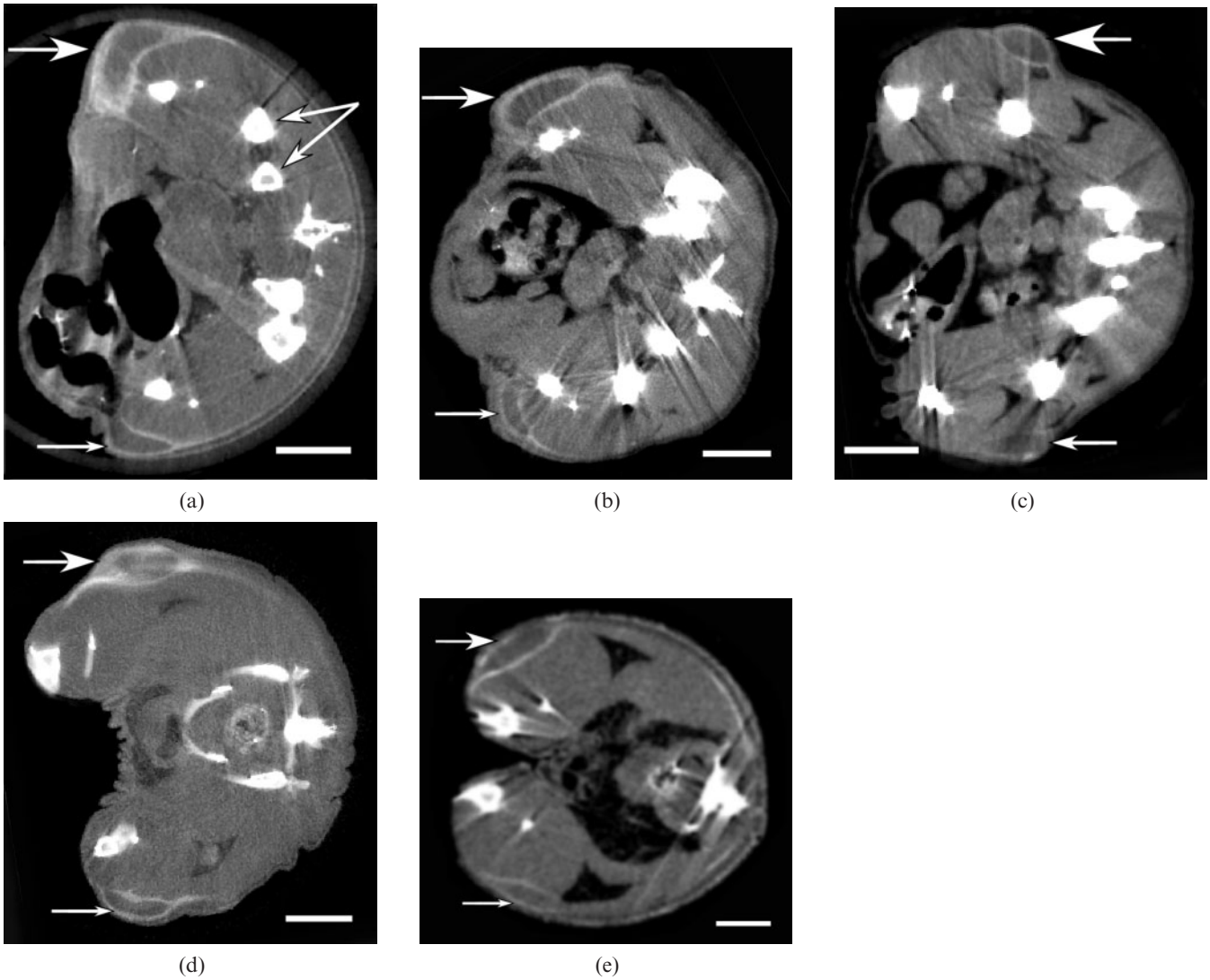

(a) (b) (c)

(d) (e)

Figure 4. Micro-CT sections from five different mice bearing Her2+ (top large arrow) and Her2– tumours (bottom small arrow) growing in opposite thighs imaged 20 h after intravenous injection of 15 nm Herceptin–AuNPs. Dose applied was (a) 1.10 g Au kg^{-1}, (b) 0.31 g Au kg^{-1}, (c) 0.57 g Au kg^{-1}, (d) 0.86 g Au kg^{-1}, (e) 0.72 g Au kg^{-1}. Double arrow in (a) points to bones. (a–c) Taken with Scanco uCT40, (d) and (e) with Scanco VivaCT40. Bar=5 mm.

Table 1. Quantification results from micro-CT measurements of mice intravenously injected with Herceptin–AuNPs. The Her2+/Her2– ratio is the Her2+ % id g^{-1} divided by the corresponding Her2– % id g^{-1} (n=5). (Muscle value is from atomic absorption measurements)

	% id $g^{-1} \pm$ SEM[a]	Her2+/Her2−	Tumour/muscle
Her2+ (whole tumour)	8.3 ± 1.3	(Whole tumour) 1.3	11.4
Her2− (whole tumour)	6.2 ± 1.6		8.5
Her2+ (periphery)	15.8 ± 1.7	(Shell) 1.6	21.8
Her2− (periphery)	10.1 ± 1.6		13.9
Her2+ (centre)	1.5 ± 0.7	(Centre) 2.2	2.1
Her2− (centre)	0.7 ± 0.7		1.0
Muscle	0.72 ± 0.14		

[a]% injected dose per gram is defined as (tumour Au concentration (mg Au g^{-1} tumour))/(total injected Au dose (mg Au)) × 100%.

Representative three-dimensional images are shown in Figure 6. Either type of imaging (planar or volumetric) enabled clear recognition of small tumours. The tumour shown in Figure 6a was only 1.5 mm thick.

Discussion

In this study, large gold doses were used to clearly demonstrate proof of principle and provide noise-free images with amounts suitable for accurate quantification so that calculations of contrast-to-noise could be made to determine detectable limits and predict performance with clinical machines. If such values are known, doses can be reduced many-fold in future studies to assess clinical relevance. While 45 kVp was chosen owing to the range available on the micro-CT unit, the lower voltages used in mammography (*e.g.* 25 kVp) and higher energies used for clinical CT (*e.g.* 140 kVp) should also produce favourable contrast from gold owing to its significantly greater attenuation coefficient than soft tissue. Appropriate beam filtering could also maximise use of gold's L-edge absorptions at 14.4, 13.7 and 11.9 keV, and K-edge absorption at 80.7 keV.

Mice were imaged 20 h after iv gold injection since IgG immunoconjugates accumulate maximally in tumours after approximately 20–24 h [20, 21]. This time period also allows the gold blood volume to dissipate, giving lower backgrounds. Animals were killed just before micro-CT imaging in order to eliminate motion for the 40 min imaging time. There is no evidence to suggest that any significant redistribution of gold occurred by this procedure compared with imaging live mice at this time.

Herceptin has a K_d of 8–14 nM and targets Her2+ tumours, such as the BT474 human breast cancer line used in this study, which has $1-2 \times 10^6$ receptors per cell [22]. MCF-7 breast cancer cells (the negative control) lack the Her2 gene amplification and only express Her2 protein at low or basal levels, approximately 10^4 Her2 receptors per cell [18]. The *in vitro* uptake we measured, 4.5×10^5 AuNPs per cell, correlates well with that found in another study, where ferritin conjugated to epidermal growth factor (EGF) yielded 5×10^5 ferritin molecules internalised after incubation with EGF-expressing A-431 human carcinoma cells [23].

In other non-CT work, Herceptin has been used for targeted imaging using radioactivity [22], radioactive liposomes [18], magnetic nanoparticles [24], gadolinium [24–26] ^{18}F-PET [27], fluorophores [28–30] and

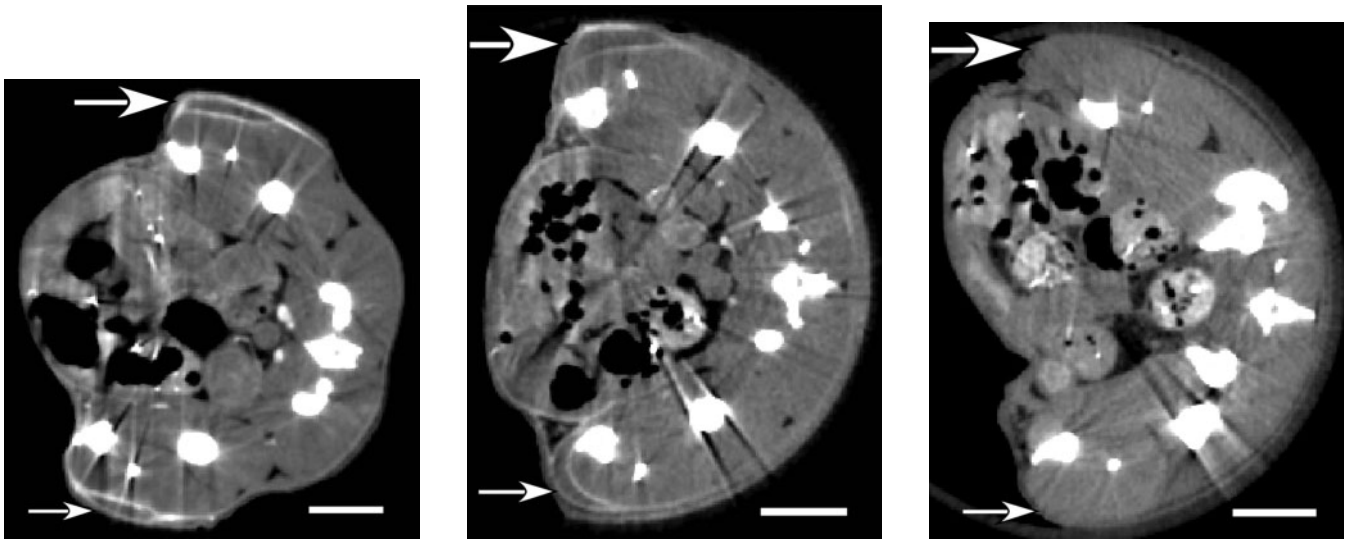

(a) (b) (c)

Figure 5. Micro-CT sections of mice injected with (a) 15 nm AuNPs only (1.1 g Au kg^{-1}); (b) 15 nm AuNPs conjugated to non-specific mouse IgG (1.1 g Au kg^{-1}); (c) no AuNP injection. Large arrow (top) points to Her2+ tumour and small arrow (bottom) points to Her2– tumour. Bar=5 mm.

Table 2. Quantification results from micro-CT measurements of mice intravenously injected with AuNPs only or non-specific IgG-AuNPs (mouse IgG)

Injectate		% id g^{-1}	Her2+/Her2−
AuNPs	Her2+ (whole tumour)	8.7	1.0
AuNPs	Her2− (whole tumour)	8.3	
AuNPs	Her2+ (periphery)	10.7	1.2
AuNPs	Her2− (periphery)	9.2	
Non-specific IgG-AuNP	Her2+ (whole tumour)	4.1	1.0
Non-specific IgG-AuNP	Her2− (whole tumour)	4.1	
Non-specific IgG-AuNP	Her2+ (periphery)	5.4	1.0
Non-specific IgG-AuNP	Her2− (periphery)	5.6	

id g^{-1}, injected dose pergram.

near-infrared probes [28, 31, 32]. Consistent with these studies, we found a tumour uptake value (8.3% id g^{-1}) similar to these other Herceptin adducts, indicating that the 15 nm AuNP–antibody conjugate delivery does not substantially alter the tumour uptake compared with, for example, a radiolabelled Herceptin antibody targeted to BT474 tumours, which showed 7.8% id g^{-1} localisation [22]. The ratio of Her2+/Her2– localisation we found in this study, 1.34, also agrees with another study using Herceptin-targeted with approximately 100 nm liposomes to the same tumour lines, which gave a Her2+/Her2– ratio of 1.16 [18].

In related work, the biodistribution of various AuNPs has been measured *in vivo* by inductively coupled plasma (ICP)-atomic emission spectroscopy, ICP-mass spectroscopy, atomic absorption spectroscopy, neutron activation, radioactivity (111-In chelates), light microscopy, transmission electron microscopy, X-ray microanalysis (EDX), gamma imaging and micro-CT [2, 33–38]. Tissue uptake was found to vary with size, shape and coating of the AuNPs. Only one of these studies [38] reported bulk tumour localisation, which showed untargeted PEG-coated 20 nm AuNPs accumulating to 6.63% id g^{-1} after 48 h in A431 subcutaneous tumours, whereas 80 nm particles only reached 0.30% id g^{-1}. This is consistent with our measurement of untargeted PEG-coated 15 nm AuNPs that showed a whole tumour uptake of 8.5% id g^{-1} (Table 2, average of Her2+ and Her2– whole tumour values), which is slightly higher than the reported 6.63% id g^{-1}, probably as a result of their smaller size or differences in tumour model. Muscle values were also consistent with these other studies. However, none of these studies reported quantitative microlocalisation of gold within tumours.

In vivo, a commonly observed phenomenon with nanoparticles is the ''enhanced permeability and retention'' (EPR) effect [39, 40]. Tumour vasculature is more permeable owing to angiogenesis, and nanoparticles tend to leak out and are retained there. Also, carcinomas have poor central circulation. This would account for the predominant accumulation at the tumour's growing edge. It would also explain both why the Her2– tumours accumulate gold and the disparity with the *in vitro* result, where the Her2+ to Her2– ratio was around 40:1 whereas the *in vivo* ratio was only 1.3 (whole tumour) or 1.6 (periphery ratio). Penetration into the tumour might be enhanced by using smaller gold particles, antibody fragments or peptides.

The contrast produced by ''untargeted'' AuNPs (tumour periphery/muscle ratio=21.8) is high enough to enable their possible use as a general-purpose aid to tumour detection during CT or mammography, since they would highlight all tumour types. We observed that AuNPs without any antibody had better tumour uptake than with a non-specific antibody attached, probably owing to the former's smaller size.

The tumours detected here were small, some were only 1.5 mm. The method should enable more certain recognition of smaller tumours than currently possible by CT and mammography. Detecting small tumours is important because it is critical to find tumours before

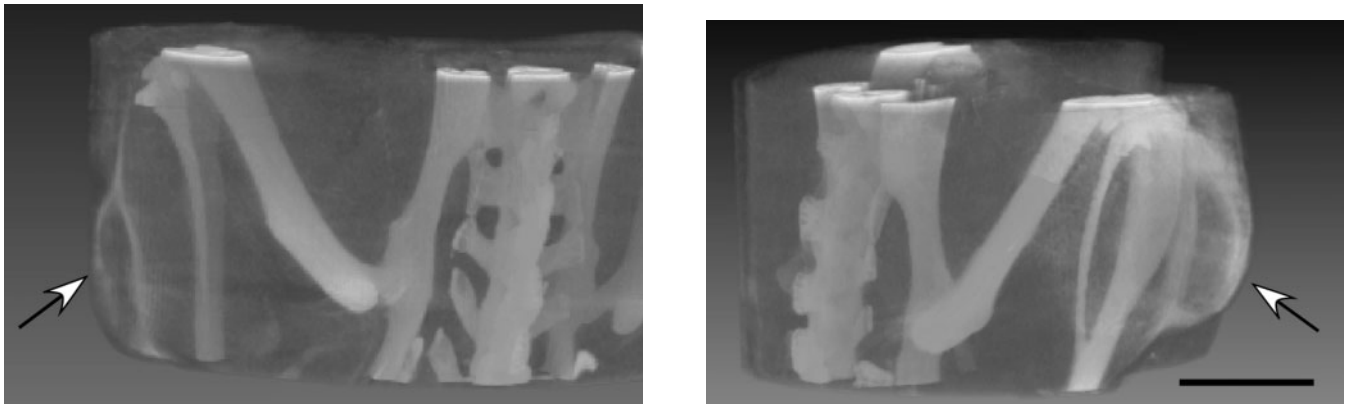

(a) (b)

Figure 6. Micro-CT volume images from animal shown in Figure 1a with Her2– (a) (arrow) and Her2+ (b) (arrow) tumours growing in opposite thighs delineated by Herceptin–AuNPs. Imaging was 20 h after intravenous injection of Herceptin–15 nm AuNPs (1.1 g Au kg^{-1}) The tumour in (a) is 1.5 mm thick. Bar=5 mm.

they grow large enough to metastasise. Although our mouse imaging was with micro-CT, it should still be possible to retain small tumour size detection with clinical CT, which currently have submillimetre instrumental resolution. The increased voltage of a clinical CT still gives excellent gold absorption contrast compared with uncontrasted soft tissue [10]. The large gold dose used here (producing 310 HU in the tumour periphery) was only for demonstration purposes, and could be reduced substantially to usable detection limits.

What then is the predicted amount of gold needed to yield useful imaging by CT in a human? The mass attenuation coefficient of gold for a typical 140 kVp CT spectrum (broad spectrum with around 70 keV mean energy) is 3.10 $cm^2 g^{-1}$ at 70 keV [19]. The linear attenuation coefficient of soft tissue is 0.19 cm^{-1} at 70 keV. Therefore, 1 mg ml^{-1} of gold produces a CT image contrast of $1000 \times 0.0031/0.19 = 16.3$ HU. Because CT scanners can detect a lesion with 8 HU contrast [41], this means that the sensitivity for gold will be about 0.5 mg ml^{-1}. Monoclonal antibody delivery in humans is typically far lower than the 5–40% id g^{-1} seen in mice. Typical values range from 0.006 to 0.03% id g^{-1} [42–44], or are 100–1000 times lower than in mice. To produce a difference of 8 HU (0.5 mg Au ml^{-1}) with 0.03% id g^{-1} delivery, 1.7 g of injected gold would be required. However, newer dual-energy and multihead CTs are able to reduce the detection levels further [45, 46]. X-ray imaging equipment that would exploit gold's favourable absorption edges would not only improve sensitivity but also reduce patient dose.

AuNPs agents have a different chemistry that may avoid kidney toxicity, which is a problem with iodine contrast agents experienced by patients with renal insufficiency. Although some AuNPs appear non-toxic at useful levels [3, 47], more testing is needed. Another advantage is the prolonged tumour contrasting (here to 20 h) compared with the more ephemeral MRI and PET contrast imaging. Knowing exact tumour topology could assist in surgery, radiation treatment planning, monitoring and other image-guided procedures. Imaging provides a potential alternative to painful and invasive biopsies that may not accurately sample the tumour. A serious problem with current surgery and radiotherapy is that the true tumour boundaries are not exactly known.

Conclusion

In summary, these results show that micro-CT can be used to quantify AuNP microlocalisation in tumours. 15 nm AuNPs were found largely confined to the tumour periphery, and, even without antibodies, provide useful CT contrast, enabling detection of small millimetre-sized tumours. When linked to tumour-specific antibodies, the AuNPs provide additional specific radiocontrast. Because of their significant targeting to tumours, AuNPs may also find uses in tumour typing, image-guided procedures, monitoring and therapies.

Acknowledgments

This work was supported by National Institutes of Health grants (R44CA108013, R44CA124190) and the Dr. med. h.c. Erwin Braun Stiftung, Basel.

J F Hainfeld is a part owner of Nanoprobes, Inc. Other authors have no financial interest.

References

1. Popovtzer R, Agrawal A, Kotov NA, Popovtzer A, Balter J, Carey TE, et al. Targeted gold nanoparticles enable molecular CT imaging of cancer. Nano Lett 2008;8:4593–6.
2. Cai QY, Kim SH, Choi KS, Kim SY, Byun SJ, Kim KW, et al. Colloidal gold nanoparticles as a blood-pool contrast agent for X-ray computed tomography in mice. Invest Radiol 2007;42:797–806.
3. Hainfeld JF, Slatkin DN, Focella TM, Smilowitz HM. Gold nanoparticles: a new X-ray contrast agent. Br J Radiol 2006;79:248–53.
4. Gobin AM, Lee MH, Halas NJ, James WD, Drezek RA, West JL. Near-infrared resonant nanoshells for combined optical imaging and photothermal cancer therapy. Nano Lett 2007;7:1929–34.
5. Qian X, Peng XH, Ansari DO, Yin-Goen Q, Chen GZ, Shin DM, et al. In vivo tumor targeting and spectroscopic detection with surface-enhanced Raman nanoparticle tags. Nat Biotechnol 2008;26:83–90.
6. Paciotti GF, Myer L, Weinreich D, Goia D, Pavel N, McLaughlin RE, et al. Colloidal gold: a novel nanoparticle vector for tumor directed drug delivery. Drug Deliv 2004;11:169–83.
7. von Maltzahn G, Park JH, Agrawal A, Bandaru NK, Das SK, Sailor MJ, et al. Computationally guided photothermal tumor therapy using long-circulating gold nanorod antennas. Cancer Res 2009;69:3892–900.
8. Hainfeld JF, Slatkin DN, Smilowitz HM. The use of gold nanoparticles to enhance radiotherapy in mice. Phys Med Biol 2004;49:N309–15.
9. Cho SH. Estimation of tumour dose enhancement due to gold nanoparticles during typical radiation treatments: a preliminary Monte Carlo study. Phys Med Biol 2005;50: N163–73.
10. Hainfeld JF, Dilmanian FA, Slatkin DN, Smilowitz HM. Radiotherapy enhancement with gold nanoparticles. J Pharm Pharmacol 2008;60:977–85.
11. McMahon SJ, Mendenhall MH, Jain S, Currell F. Radiotherapy in the presence of contrast agents: a general figure of merit and its application to gold nanoparticles. Phys Med Biol 2008;53:5635–51.
12. Pietras RJ, Fendly BM, Chazin VR, Pegram MD, Howell SB, Slamon DJ. Antibody to HER-2/neu receptor blocks DNA repair after cisplatin in human breast and ovarian cancer cells. Oncogene 1994;9:1829–38.
13. Frens G. Controlled nucleation for the regulation of the particle size in monodisperse gold suspensions. Nature Phys Res 1973;241:20–2.
14. Takae S, Akiyama Y, Otsuka H, Nakamura T, Nagasaki Y, Kataoka K. Ligand density effect on biorecognition by PEGylated gold nanoparticles: regulated interaction of RCA120 lectin with lactose installed to the distal end of tethered PEG strands on gold surface. Biomacromolecules 2005;6:818–24.
15. Cuatrecasas P, Parikh I. Adsorbents for affinity chromatography. Use of N-hydroxysuccinimide esters of agarose. Biochemistry 1972;11:2291–9.
16. Wise PM, Camp-Grossman P, Barraclough CA. Effects of estradiol and progesterone on plasma gonadotropins, prolactin, and LHRH in specific brain areas of ovariectomized rats. Biol Reprod 1981;24:820–30.
17. Dubal DB, Wise PM. Neuroprotective effects of estradiol in middle-aged female rats. Endocrinology 2001;142:43–8.
18. Kirpotin DB, Drummond DC, Shao Y, Shalaby MR, Hong K, Nielsen UB, et al. Antibody targeting of long-circulating lipidic nanoparticles does not increase tumor localisation

but does increase internalisation in animal models. Cancer Res 2006;66:6732–40.
19. Hubbell JH, Seltzer SM. Tables of X-ray mass attenuation coefficients and mass energy-absorption coefficients. 1996. Accessed 3 May 2009. Available from: http://physics.nist.gov/PhysRefData/XrayMassCoef/tab4.html.
20. Andrew SM, Johnstone RW, Russell SM, McKenzie IF, Pietersz GA. Comparison of in vitro cell binding characteristics of four monoclonal antibodies and their individual tumor localisation properties in mice. Cancer Res 1990;50:4423–8.
21. Grunberg J, Novak-Hofer I, Honer M, Zimmermann K, Knogler K, Blauenstein P, et al. In vivo evaluation of 177Lu- and 67/64Cu-labeled recombinant fragments of antibody chCE7 for radioimmunotherapy and PET imaging of L1-CAM-positive tumors. Clin Cancer Res 2005;11:5112–20.
22. Tang Y, Wang J, Scollard DA, Mondal H, Holloway C, Kahn HJ, et al. Imaging of HER2/neu-positive BT-474 human breast cancer xenografts in athymic mice using (111)In-trastuzumab (Herceptin) Fab fragments. Nucl Med Biol 2005;32:51–8.
23. Haigler HT, McKanna JA, Cohen S. Direct visualisation of the binding and internalisation of a ferritin conjugate of epidermal growth factor in human carcinoma cells A-431. J Cell Biol 1979;81:382–95.
24. Wuang SC, Neoh KG, Kang ET, Pack DW, Leckband DE. HER-2-mediated endocytosis of magnetic nanospheres and the implications in cell targeting and particle magnetisation. Biomaterials 2008;29:2270–9.
25. Chong HS, Song HA, Ma X, Milenic DE, Brady ED, Lim S, et al. Novel bimodal bifunctional ligands for radioimmunotherapy and targeted MRI. Bioconjug Chem 2008;19:1439–47.
26. Zhu W, Okollie B, Bhujwalla ZM, Artemov D. PAMAM dendrimer-based contrast agents for MR imaging of Her-2/neu receptors by a three-step pretargeting approach. Magn Reson Med 2008;59:679–85.
27. Cheng Z, De Jesus OP, Namavari M, De A, Levi J, Webster JM, et al. Small-animal PET imaging of human epidermal growth factor receptor type 2 expression with site-specific 18F-labeled protein scaffold molecules. J Nucl Med 2008;49:804–13.
28. Lee SB, Hassan M, Fisher R, Chertov O, Chernomordik V, Kramer-Marek G, et al. Affibody molecules for in vivo characterization of *HER2*-positive tumors by near-infrared imaging. Clin Cancer Res 2008;14:3840–9.
29. Takeda M, Tada H, Higuchi H, Kobayashi Y, Kobayashi M, Sakurai Y, et al. In vivo single molecular imaging and sentinel node navigation by nanotechnology for molecular targeting drug-delivery systems and tailor-made medicine. Breast Cancer 2008;15:145–52.
30. Koyama Y, Barrett T, Hama Y, Ravizzini G, Choyke PL, Kobayashi H. In vivo molecular imaging to diagnose and subtype tumors through receptor-targeted optically labeled monoclonal antibodies. Neoplasia 2007;9:1021–9.
31. Bhattacharyya S, Wang S, Reinecke D, Kiser W, Jr., Kruger RA, DeGrado TR. Synthesis and evaluation of near-infrared (NIR) dye-herceptin conjugates as photoacoustic computed tomography (PCT) probes for HER2 expression in breast cancer. Bioconjug Chem 2008;19:1186–93.
32. Welsher K, Liu Z, Daranciang D, Dai H. Selective probing and imaging of cells with single walled carbon nanotubes as near-infrared fluorescent molecules. Nano Lett 2008;8:586–90.
33. Hillyer JF, Albrecht RM. Correlative instrumental neutron activation analysis, light microscopy, transmission electron microscopy, and X-ray microanalysis for qualitative and quantitative detection of colloidal gold spheres in biological specimens. Microsc Microanal 1998;4:481–90.
34. Hillyer JF, Albrecht RM. Gastrointestinal persorption and tissue distribution of differently sized colloidal gold nanoparticles. J Pharm Sci 2001;90:1927–36.
35. Niidome T, Yamagata M, Okamoto Y, Akiyama Y, Takahashi H, Kawano T, et al. PEG-modified gold nanorods with a stealth character for in vivo applications. J Control Release 2006;114:343–7.
36. Sonavane G, Tomoda K, Makino K. Biodistribution of colloidal gold nanoparticles after intravenous administration: effect of particle size. Colloids Surf B Biointerfaces 2008;66:274–80.
37. Terentyuk GS, Maslyakova GN, Suleymanova LV, Khlebtsov BN, Kogan BY, Akchurin GG, et al. Circulation and distribution of gold nanoparticles and induced alterations of tissue morphology at intravenous particle delivery. J Biophotonics 2009;2:292–302.
38. Zhang G, Yang Z, Lu W, Zhang R, Huang Q, Tian M, et al. Influence of anchoring ligands and particle size on the colloidal stability and in vivo biodistribution of polyethylene glycol-coated gold nanoparticles in tumor-xenografted mice. Biomaterials 2009;30:1928–36.
39. Noguchi Y, Wu J, Duncan R, Strohalm J, Ulbrich K, Akaike T, et al. Early phase tumor accumulation of macromolecules: a great difference in clearance rate between tumor and normal tissues. Jpn J Cancer Res 1998;89:307–14.
40. Dvorak HF, Nagy JA, Dvorak JT, Dvorak AM. Identification and characterisation of the blood vessels of solid tumors that are leaky to circulating macromolecules. Am J Pathol 1988;133:95–109.
41. Paulus MJ, Gleason SS, Kennel SJ, Hunsicker PR, Johnson DK. High resolution X-ray computed tomography: an emerging tool for small animal cancer research. Neoplasia 2000;2:62–70.
42. Scott AM, Lee FT, Jones R, Hopkins W, MacGregor D, Cebon JS, et al. A phase I trial of humanized monoclonal antibody A33 in patients with colorectal carcinoma: biodistribution, pharmacokinetics, and quantitative tumor uptake. Clin Cancer Res 2005;11:4810–17.
43. Storto G, Buchegger F, Waibel R, Kuenzi G, Offord RE, Schubiger PA, et al. Biokinetics of a F(ab')3 iodine-131 labeled antigen binding construct (Mab 35) directed against CEA in patients with colorectal carcinoma. Cancer Biother Radiopharm 2001;16:371–9.
44. Beatty JD, Duda RB, Williams LE, Sheibani K, Paxton RJ, Beatty BG, et al. Preoperative imaging of colorectal carcinoma with 111In-labeled anticarcinoembryonic antigen monoclonal antibody. Cancer Res 1986;46:6494–502.
45. Takahashi N, Hartman RP, Vrtiska TJ, Kawashima A, Primak AN, Dzyubak OP, et al. Dual-energy CT iodine-subtraction virtual unenhanced technique to detect urinary stones in an iodine-filled collecting system: a phantom study. AJR Am J Roentgenol 2008;190:1169–73.
46. Wang ZJ, Coakley FV, Fu Y, Joe BN, Prevrhal S, Landeras LA, et al. Renal cyst pseudoenhancement at multidetector CT: what are the effects of number of detectors and peak tube voltage? Radiology 2008;248:910–16.
47. Nie S, Xing Y, Kim GJ, Simons JW. Nanotechnology applications in cancer. Annu Rev Biomed Eng 2007;9:257–88.